UCRL-CONF-212745

LAWRENCE
LIVERMORE
NATIONAL
LABORATORY

Advanced Techniques for In-Situ Monitoring of Phase Transformations During Welding Using Synchrotron-Based X-Ray Diffraction

J. W. Elmer, T. A. Palmer, W. Zhang, T. DebRoy

June 7, 2005

7th International Trends in Welding
Pine Mountain, GA, United States
May 16, 2005 through May 20, 2005

Disclaimer

This document was prepared as an account of work sponsored by an agency of the United States Government. Neither the United States Government nor the University of California nor any of their employees, makes any warranty, express or implied, or assumes any legal liability or responsibility for the accuracy, completeness, or usefulness of any information, apparatus, product, or process disclosed, or represents that its use would not infringe privately owned rights. Reference herein to any specific commercial product, process, or service by trade name, trademark, manufacturer, or otherwise, does not necessarily constitute or imply its endorsement, recommendation, or favoring by the United States Government or the University of California. The views and opinions of authors expressed herein do not necessarily state or reflect those of the United States Government or the University of California, and shall not be used for advertising or product endorsement purposes.

Advanced Techniques for In-Situ Monitoring of Phase Transformations During Welding Using Synchrotron-Based X-Ray Diffraction

J. W. Elmer, T. A. Palmer
Lawrence Livermore National Laboratory, Livermore, California, USA

W. Zhang, T. DebRoy
The Pennsylvania State University, University Park, Pennsylvania, USA

Abstract

Understanding the evolution of microstructure in welds is an important goal of welding research because of the strong correlation between weld microstructure and weld properties. To achieve this goal it is important to develop a quantitative measure of phase transformations encountered during welding in order to ultimately develop methods for predicting weld microstructures from the characteristics of the welding process. To aid in this effort, synchrotron radiation methods have been developed at Lawrence Livermore National Laboratory (LLNL) for direct observation of microstructure evolution during welding. Using intense, highly collimated synchrotron radiation, the atomic structure of the weld heat affected and fusion zones can be probed in real time. Two synchrotron-based techniques, known as spatially resolved (SRXRD) and time resolved (TRXRD) x-ray diffraction, have been developed for these investigations. These techniques have now been used to investigate welding induced phase transformations in titanium alloys, low alloy steels, and stainless steel alloys. This paper will provide a brief overview of these methods and will discuss microstructural evolution during the welding of low carbon (AISI 1005) and medium carbon (AISI 1045) steels where the different levels of carbon influence the evolution of microstructures during welding.

Introduction

Over the past several years an experimental technique utilizing synchrotron radiation has been developed at LLNL to directly observe phase transformations during the welding of commercial alloys. Many orders of magnitude more powerful than conventional x-rays, this intense form of radiation is the result of the deflection of highly energetic, charged particles, traveling at nearly the speed of light, by a strong magnetic field. The resulting electromagnetic radiation emitted by these particles is passed between an array of powerful magnetic poles, called a wiggler, to further increase the x-ray intensity. This intense, highly collimated radiation can be used to probe atomic structures in time scales of milliseconds, making possible the real-time observation of phase transformations during welding. The synchrotron technique is now being used to provide information about welding-induced phase transformations that cannot be obtained by conventional characterization methods.

Traditional characterization methods are limited by their inability to provide direct information about the weld microstructure as it evolves. For example, post-weld microstructural characterization provides only a snapshot of the last stage in a series of phase transformations. No information about the evolution of the microstructure or the rates of the intermediate phase transformations is obtained. Other experimental methods traditionally used to study phase transformation kinetics, such as dilatometry and differential scanning calorimetry, are indirect in that they measure changes in sample length or enthalpy, but do not directly determine the phases that are present at elevated temperatures. In addition, these techniques oftentimes can not duplicate the steep thermal gradients and high peak temperatures experienced during welding. As a result of these inherent experimental difficulties, quantitative kinetic data pertaining to welding induced phase transformations in steels and other important commercial alloys remains scarce.

To overcome the limitations of traditional weld characterization techniques, two types of synchrotron-based experiments have been developed at LLNL to take advantage of the high energy x-rays. In the first type of experiment, x-ray diffraction patterns are acquired in real time during welding using a sub-mm sized x-ray beam. These patterns are acquired at discreet locations along a linear scan beginning in the weld fusion zone, proceeding through the weld Heat Affected Zone (HAZ), and ending in the base metal. These spatially resolved x-ray diffraction experiments (SRXRD) allow the phase transformations occurring over a range of locations in the weld HAZ to be monitored during steady state welding conditions. In the second technique, x-ray diffraction patterns are again acquired in real time, but they are acquired at very short time intervals during welding at a single location during a transient spot weld, again using sub-mm sized beams. The time resolved x-ray diffraction technique (TRXRD) allows the evolution of a phase transformation to be monitored with high temporal resolution (10 to 100 ms) during rapid weld heating and cooling conditions. The combination of these two techniques provides a one-of-a-kind capability for

the real time monitoring of phase transformation kinetics during welding.

These techniques have been used to understand phase transformations during welding of a large number of alloys, including steels [1-5], and welding filler metals [6, 7]. These data have further been used to develop kinetic models to predict weld phase transformations for different welding conditions [8-11]. This article provides a brief overview of recent results, showing new kinetic information about the $\alpha \rightarrow \gamma$ transformation during weld heating, and the first direct observations of bainitic and martensitic transformations during weld cooling.

Materials and Experimental Procedures

Gas tungsten arc (GTA) welds were made on cylindrical bar samples while performing in-situ observations of the phase transformations that occurred during the weld. The GTA welds were made at approximately 2kW power levels, and were moving at speeds on the order of 1.0 mm/s. These parameters produced welds approximately 10 mm wide and 5 mm deep. The samples used for the experiments were machined from 10.8 cm diameter forged bar stock to produce solid cylinders that measured 12.7 cm long and 10.2 cm diameter. The welds were made on the cylindrical bars inside an environmentally sealed chamber that was pumped down to vacuum conditions before backfilling with high purity helium prior to welding. The helium prevented atmospheric contamination of the weld, and minimized attenuation of the x-ray beam. Details of similar welding experiments are reported elsewhere [1, 2, 4, 8].

Fig. 1 shows a schematic drawing of the major components of the experimental setup used for the SRXRD and TRXRD experiments. In each experiment, the x-ray beam passes through a monochromator (not shown) before passing through a tungsten pinhole. This produces a monoenergetic and sub-millimeter sized beam, which impinges on the sample at a given location. In the SRXRD experiment (shown), discreet HAZ locations are analyzed along the path perpendicular to the weld direction with 250 μm precision. In the TRXRD experiment, a single location is probed during spot welding on a stationary bar, allowing the temporal evolution of phase to be investigated with a 50ms temporal resolution.

The in-situ x-ray diffraction experiments are performed using the 31-pole wiggler beam line, BL 10-2 at Stanford Synchrotron Radiation Laboratory (SSRL) with SPEAR (Stanford Positron-Electron Accumulation Ring) operating at an electron energy of 3.0 GeV and an injection current of ~100 mA. The focused monochromatic synchrotron x-ray beam is passed through a tungsten pinhole, 250 μm (SRXRD) or 540 μm (TRXRD), to render a sub-millimeter beam on the sample at an incident angle of ~25°. This setup yielded a beam flux on the sample of ~10^{12} photons/s, which was determined experimentally using an ion chamber immediately downstream from the pinhole. A photon energy of 12.0 keV (λ = 0.1033 nm) was chosen to facilitate phase identification and to be far enough in energy above the Fe K-edge (7.112 keV) to minimize the background contribution due to Fe K-fluorescence from the steel samples.

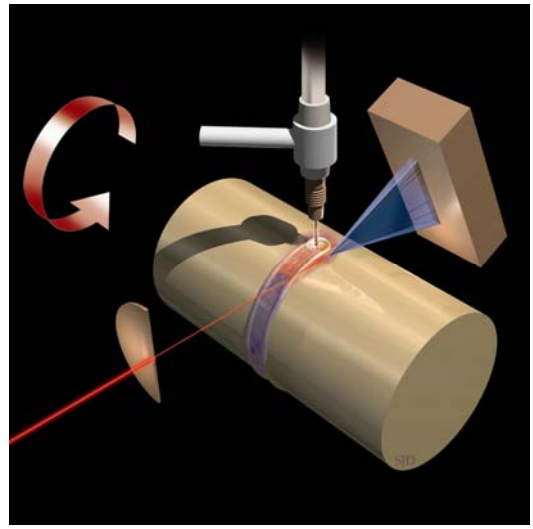

Fig. 1: Schematic diagram of the experimental setup used for SRXRD in-situ observations of phase transformations during welding using synchrotron radiation. TRXRD uses the same setup on a stationary bar.

The x-ray diffraction patterns were recorded using a 50 mm long 2048 element position sensitive Si photodiode array detector. The array was mounted on a dual-stage water cooled Peltier effect thermoelectric cooler at a location approximately 10 cm behind the weld to cover a 2θ range from 22° to 52°. This 2θ range was optimized to contain a total of six diffraction peaks, three from the bcc phase (α-Fe) and three from the fcc phase (γ-Fe). Calibration of the x-ray diffraction patterns was performed using a thin niobium foil, which has a well characterized bcc crystal structure. Other details about the experimental setup can be found in previous publications [1-3].

Modeling and Analysis

Diffraction Peak Analysis The x-ray diffraction patterns gathered during the welding experiments were analyzed to determine the phases present and the semi-quantitative volume fractions of each phase. This analysis measured the integrated intensity of the peaks in each diffraction pattern using a sum of one or more Gaussian peak profile fitting functions [12, 13]. The area and FWHM values of the fitted peaks were then determined using an automated curve-fitting routine developed in Igor Pro®, Version 4.0 [8, 14].

The raw integrated intensities of the diffraction peaks were then converted into relative phase intensities. This conversion is based on the effects of a number of factors on the resulting intensity of a given peak. In this method, the peak area or

integrated intensity of each peak is measured and then converted to relative fraction of each phase by considering the crystal structure, the Lorentz polarization factor, and the temperature. The overall methodology used is described elsewhere [8].

Thermal Modeling Direct measurement of weld temperatures is very difficult, particularly during in-situ experiments such as these. To overcome this, weld thermal cycles were calculated, instead of measured, for both the SRXRD and TRXRD experiments. These calculations were used to determine the weld temperature as a function of position (SRXRD), and as a function of time at a given position (TRXRD). The weld model was developed by the Pennsylvania State University, and utilizes a 3D numerical heat transfer and fluid flow code that was created specifically for welds [8-10]. The model solves the equations of conservation of mass, momentum and energy in three-dimensional form to determine the size and shape of the liquid weld pool. In the SRXRD experiments, the thermal profile in the steady state weld pool and in the HAZ was determined for the for the quasi steady state welding condition. In the TRXRD experiments, the thermal profile was determined as a function of time and position for the transient spot welding conditions. The mathematical formulation of these models is discussed in detail in the references [15-17]. Applications of the coupled thermal-fluids model for the steady state welds used for SRXRD are discussed in references [5, 8-10], while the application of this model to the transient welds used in the TRXRD experiments are discussed in references [11, 18].

Phase Equilibria Thermocalc was used to calculate the phase transformation sequence for the 1005 and 1045 steel alloys [19]. These calculations show the transformation temperatures for the steels used in this investigation by considering the effects of Fe, C, Si, Mn, Ni and Cr on the liquid, ferrite, austenite, and cementite phase fields. The phase-boundary temperatures are calculated using Thermocalc for both multi-component alloys. A pseudo-binary diagram based on these calculations is shown in Fig. 2, where the compositions of the 1005 and 1045 steels are indicated.

The thermodynamic calculations indicate that the equilibrium starting microstructure for both steels will consist of a mixture of ferrite and Fe_3C (cementite) carbide phases. During heating, the microstructure of these steels will begin to transform to austenite when the A1 temperature is reached 720ºC/712ºC (1005/1045 steel). Complete transformation to austenite will occur at the A3 temperature is reached 882ºC /765ºC (1005/1045 steel), and this austenite will remain stable until melting begins to occur at 1506ºC/1410ºC (1005/1045 steel). In addition, the 1005 steel will pass through the high temperature δ phase field, which begins at a temperature of 1462ºC on heating. The 1045 steel on the other hand, is not predicted to pass through the high temperature δ phase field, so no δ ferrite should be observed.

The transformations that occur during heating will be reversed during cooling. However, kinetic limitations may affect the predicted start and completion temperatures of the phase transformations, and the formation of non-equilibrium phases such as bainite and/or martensite may occur if the cooling rates are high enough.

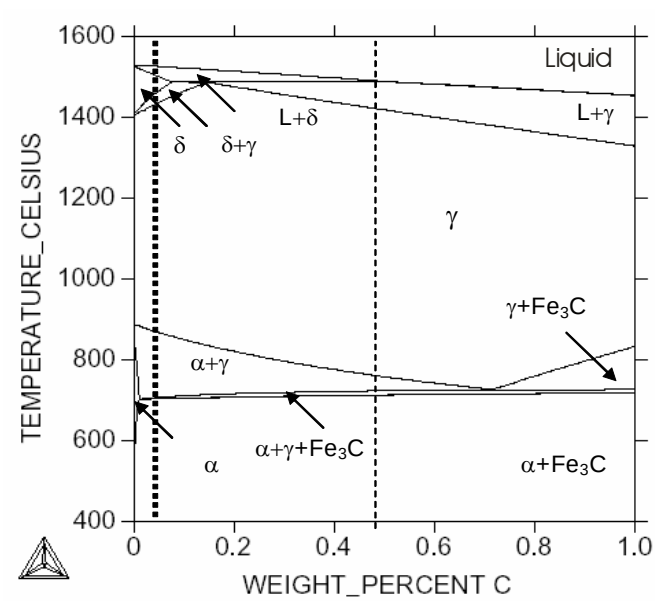

Fig. 2: Thermodynamically calculated pseudobinary diagram for C-Mn steels. Compositions of the 1005 steel (left) and 1045 steel (right) are indicated by the vertical dashed lines.

Results and Discussion

SRXRD Phase Mapping of 1005 and 1045 Steels The carbon content of steels strongly affects both the starting microstructure of the base metal and the evolution of microstructures during welding. In this portion of the paper, the phase transformations that occur in these two steels will be described based on the results of the SRXRD experiments that mapped the HAZ phase transformations during welding. Since both the amount and distribution of these carbides influence the kinetics of the $\alpha \rightarrow \gamma$ transformation, the evolution of microstructures during welding would be expected to be different for these two steels.

For very low carbon steels, such as AISI 1005, the phase transformations that occur are similar to those for pure Fe, except for the formation of carbides at low temperatures. These carbides are concentrated in small regions of pearlite (α+Fe_3C) located at grain boundary edges and corners, as shown in Fig. 3. The ferrite grain size of this steel was measured to be 21.5 μm [8].

The microstructure and phase transformations for the 1045 steel are more complicated. Fig. 4 shows this microstructure, which contains allotriomorphic ferrite and pearlite. The ferrite is the light etching phase that

outlines the prior austenite grain boundaries, and the pearlite is the dark etching component within. Measurements show that this microstruture contains 12% allotriomorphic ferrite, and 88% pearlite [18]. The prior austenite grain size is 92.8 μm, and the size of the allotriomorphic grain boundary ferrite phase was shown to be 15 μm to 20 μm wide on average, with some patches reaching 30 μm or more in places.

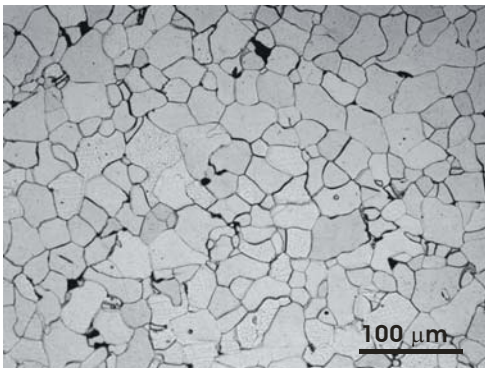

Fig. 3: Typical base metal microstructure in the 1005 steel. The dark etching pearlite is mainly at the grain boundaries.

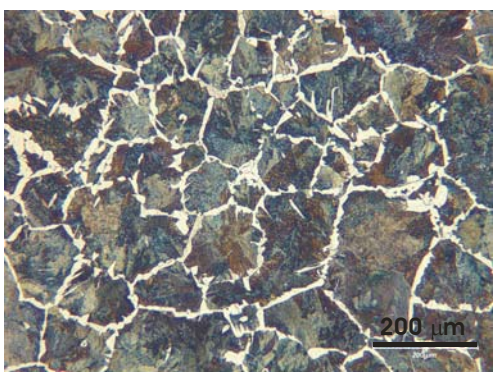

Fig.4: Base metal microstructure of the 1045 steel showing prior austenite grains and pearlite colonies inside the grains.

Transformations were observed in the HAZ of each of these steels during welding using SRXRD phase mapping. To do this, diffraction patterns were acquired in rows perpendicular to the direction of the weld as detailed in references [2, 8]. Each diffraction pattern was acquired in 0.25 mm increments, and each row of data contained more than 30 individual x-ray patterns. Twenty or more rows of data were required to complete a phase map, which shows the spatial distribution of the phases relative to the centerline of the weld. The x-ray diffraction peaks were analyzed using peak area based methods specifically in the two phase regions, to estimate the relative volume fractions of α and γ at each location in the HAZ using the technique detailed in reference [8]. The resulting data contains semi-quantitative information about the relative amounts of ferrite and austenite that existed in the weld HAZ during welding.

The final map for the 1005 steel is shown in Fig. 5, showing the volume fraction of austenite present at each weld location [8]. The shading of each point corresponds to the gradient in the volume fraction of the austenite phase, which varies from 0% austenite (blue) to 100% austenite (red). The isotherms superimpose on Fig. 5 were calculated from the coupled thermal fluids numerical code [8, 15, 16]. These isotherms correspond to the γ/(γ+δ) boundary (1432°C), the γ/(γ+α) boundary (882°C), and the Fe_3C/(α+γ) eutectoid boundary (720°C).

Note that the high temperature δ ferrite phase was observed in the 1005 steel at locations adjacent to the weld pool. This is the phase that was predicted from thermodynamics, but has never been directly observed before during welding. Another observation from this map is that the austenite transformed to ferrite during cooling at temperatures just below the A3, indicating that no martensite or bainite was produced since these transformations would not start until temperatures well below the A1 temperature. Therefore, this γ→α transformation is occurring by the nucleation and growth of ferrite from the prior austenite grain boundaries which was confirmed metallographically [2].

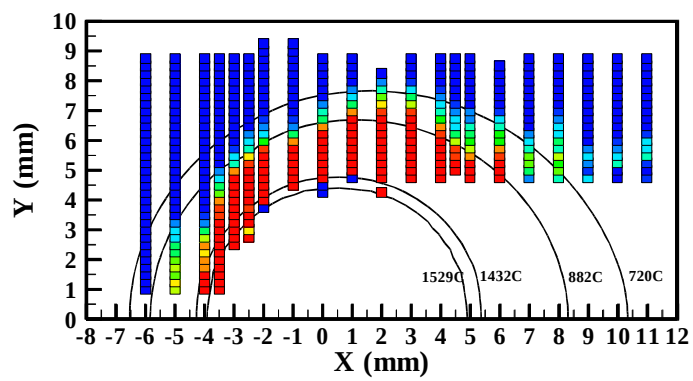

Fig. 5: SRXRD semi-quantitative map showing the volume fraction of austenite in the weld 1005 steel HAZ. In this map, weld symmetry is assumed about the centerline of the weld, and the center of the weld pool is located at x=0, y=0.

The same SRXRD mapping technique was used to observe the phase transformations in the HAZ during welding of the 1045 steel. This map was created showing the relative fractions of austenite and ferrite in the weld HAZ during welding, and these results are shown in Fig 6. In this figure, the blue shading indicates ferrite and red indicates austenite. Two calculated isotherms are plotted corresponding to the liquidus (1494°C) and the solidus (1421°C), and additional thermal modeling of the HAZ is being performed. Just as with the 1005 steel, the austenite phase field is relatively wide, extending several millimeters from the liquid boundary into the HAZ. A transition region, where ferrite and austenite coexist surrounds the austenite phase field for approximately 1 mm before reaching the single phase ferrite region of the HAZ.

The kinetics of the 1045 steel based on this map are currently being investigated, however, it is clear that there is one significant difference between the two maps. During cooling of the 1045 steel, the austenite phase field appears to extend further behind the weld in a 2 mm zone adjacent to the fusion boundary, than at locations further away from the fusion line. This extension of the austenite phase field indicates that the $\gamma \rightarrow \alpha$ phase transformation on cooling is being delayed to temperatures well below the A1adjacent to the fusion line. If this is the case, then it is likely that the cooling transformation in the HAZ adjacent to the fusion line is occurring by a bainitic or martensitic transformation. This transformation was not observed in the 1005 steel, and this comparison shows the effect of carbon content on the microstructural evolution during welding of steels.

Another observation is that 1045 steel does not indicate the presence of δ ferrite at the fusion zone boundary during welding. This is consistent with the thermodynamic calculations shown in Fig. 2. The absence of δ ferrite at the liquid/solid boundary of the weld pool in the 1045 steel weld will provide different solidification conditions than that of the 1005 steel weld where δ ferrite was present.

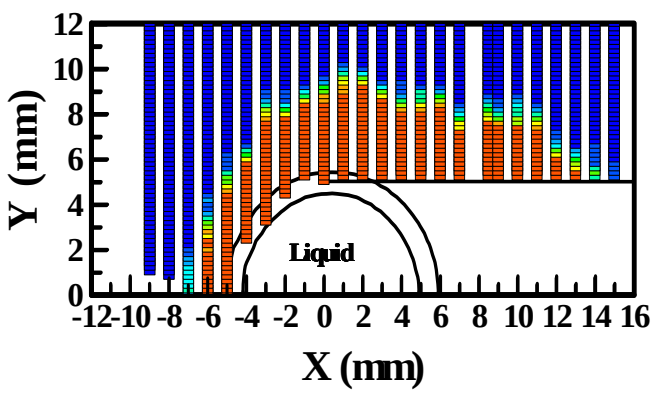

Fig. 6: SRXRD semi-quantitative map showing the volume fraction of austenite (red) in the 1045 steel HAZ. The calculated liquidus and solidus isotherms are superimpoised.

Kinetics of $\alpha \rightarrow \gamma$ Phase Transformations in AISI 1005 Steel

The phase distribution map and calculated isotherms shown in Figures 5 and 6 represent unique information regarding phase transformations in steels during welding. By combining the phase mapping results with transport phenomena based modeling, the kinetics of the phase transformations can be quantitatively determined.

In order to model the phase transformation kinetics, the Johnson-Mehl-Avrami (JMA) approach was used to describe the overall transformation rate. This approach can be represented by the following expression [20]:

$$f_e(t) = 1 - \exp\{-(kt)^n\} \qquad \text{(eq. 1)}$$

where $f_e(t)$ is the extent of the transformation at a given time t, n is the JMA exponent, and k is a rate constant given as:

$$k = k_0 \exp(-\frac{Q}{RT}) \qquad \text{(eq. 2)}$$

where k_0 is a pre-exponential constant, Q is the activation energy of the transformation including the driving forces for both nucleation and growth, R is the gas constant and T is the absolute temperature (K).

These equations were further modified [8] to derive the JMA-based expression applicable to non-isothermal phase transformations occurring in the $\alpha+\gamma$ two phase region of the HAZ. This modeling approach was combined with the calculated thermal profiles and the SRXRD experimental data to determine the JMA parameters n and k_0 for the given value of Q using a numerical fitting routine applied to the SRXRD data [9,10].

Using an assumed value for Q=117.1 kJ/mole for the activation energy of the $\alpha \rightarrow \gamma$ transformation [21], the JMA parameters for the 1005 steel were found to be $\ln(k_0)$=12.2 and n=1.45. The value of n=1.45 is consistent with diffusion controlled growth under a zero or low nucleation rate [20]. This phase transformation mechanism would imply that the preexisting pearlite regions and grain boundaries in the base metal provide the majority of the nucleation sites required for the $\alpha \rightarrow \gamma$ transformation to proceed.

More recently, this same data was analyzed using a Genetic Algorithm optimization technique to allow all three JMA parameters to be determined without making any assumptions about the activation energy parameter [22]. The results of this study modified the JMA parameters for 1005 steel, giving the new recommended parameters of Q equal to 99.9 kJ/mol, n equal to 1.12, and $\ln(k_0)$ equal to 11.06. These parameters show a better fit to the SRXRD experimental data for 1005 steel than the previous set that was determined by a graphical means and an assumed activations energy for the $\alpha \rightarrow \gamma$ phase transformation.

Using JMA kinetic parameters from the SRXRD results, time-temperature-transformation (TTT) and continuous-heating-transformation (CHT) diagrams can be constructed for the $\alpha \rightarrow \gamma$ transformation [8]. The results of the TTT calculations for the 1005 steel are shown in Fig. 7. In this plot, the constant transformation lines are compared to the A1 and A3 temperatures for this steel. As shown in this figure, the $\alpha \rightarrow \gamma$ transformation kinetics accelerate rapidly as the temperature increases. The fast rate results from the increase in both the diving force and the diffusivity of carbon in austenite with temperature. Moreover, the transformation can go to completion only at a temperature higher than the A3 temperature. The calculated TTT diagram also indicates that for the isothermal formation of austenite, the transformation start time is usually less than 1s, while the time for completion is less than 2s.

The CHT diagram shown in Fig. 8 was constructed in a similar fashion, but using constant heating rate assumptions. The transformation lines are again compared to the A1 and A3 temperatures. As shown in this figure, the transformation rate accelerates rapidly with temperature, and the start and finish temperatures for the transformation increase with increasing heating rate.

Thus kinetic parameters and transformation diagrams can be determined to predict microstructural evolution during welding. Data such as these are not readily available in the literature, and can be used to verify numerical weld models. One example is in reference [5] where the SRXRD data was further coupled with grain Monte-Carlo based growth models and cooling transformation models to predict the complete sequence of phase transformations that occur in the HAZ during welding of 1005 steel. In this work, 1005 steel arc welds were modeled using $\alpha \rightarrow \gamma$ phase transformation kinetics from the SRXRD results to determine the conditions where rapid grain growth could occur. The final grain size distribution in the weld HAZ was calculated using this integrated microstructural evolution model and compared favorably to the experimental values.

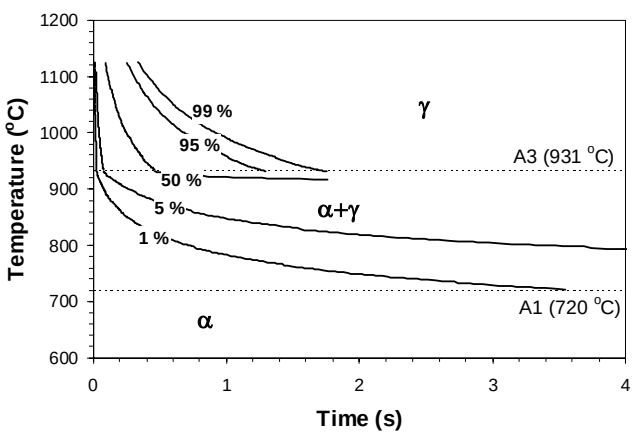

Fig. 7: TTT diagram calculated from the SRXRD data for $\alpha \rightarrow \gamma$ transformation during heating of 1005 steel.

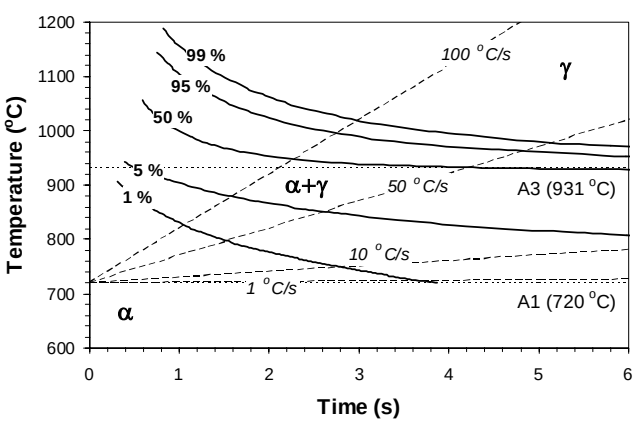

Fig. 8: CHT diagram calculated from the SRXRD results for $\alpha \rightarrow \gamma$ transformation during heating of 1005 steel.

TRXRD Experiments: Phase Transformations in 1045 Steel at High Heating and Cooling Rates. TRXRD investigations of the 1045 steel (0.45 wt% C) produced a series of x-ray diffraction patterns revealing the changes in the crystal structure at a single location in the weld HAZ during rapid heating and cooling as detailed in reference [23]. The microstructure of the 1045 steel base metal was shown in Fig. 4. Ferrite, which is the light etching phase, outlines the prior austenite grain boundaries. Inside these grains, the microstructure consists of dark etching pearlitic colonies, which occupy the majority of the microstructure.

In the TRXRD experiments performed on this steel, the x-ray beam was placed at a single pre-determined location in the HAZ during welding, 5 mm from the center of the weld. This location was selected so that during the experiment, the beam would be observing HAZ transformations to temperatures close to the melting point of the steel. In-situ diffraction patterns were recorded at this location over a sufficient amount of time so that the entire heating and cooling cycle of the weld could be captured (up to 60s).

The resulting TRXRD x-ray diffraction data are summarized in Fig. 9, in a pseudo-color format with time increasing along the y-axis, and the 2θ diffraction angle on the x-axis. In this figure, the baseline diffraction data is shown for several seconds before the arc was turned on. After arc initiation, the arc was held on for 17s during heating, and for an additional 20s during cooling after the arc was extinguished. In this figure, the higher diffraction peak intensity is indicated by the light tones, and lower peak intensities are indicated by dark tones, so that the diffraction peaks appear as streaks along the time axis at their appropriate 2θ locations.

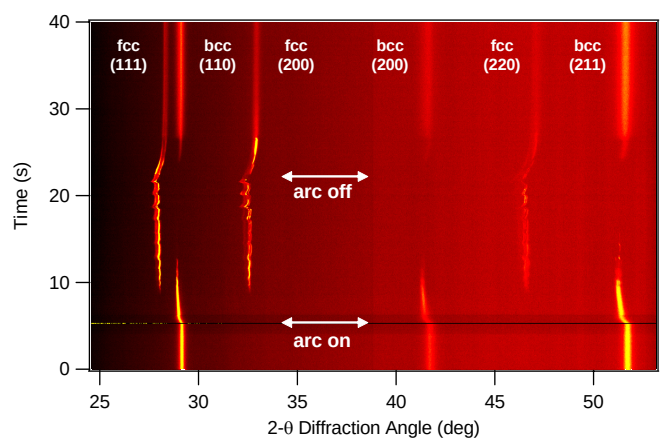

Fig 9: TRXRD results showing the changes in the diffraction peak locations as a function of welding time.

At the beginning of the experiment (t=0), only three diffraction peaks exist, corresponding to the bcc phase. After the arc is turned on, these three peaks rapidly shift to lower 2θ values as the crystal lattice of the steel expands during heating. With continued heating, three new peaks, corresponding to the

fcc phase, appear. All six peaks coexisted for several seconds before the bcc peaks began to fade in intensity and dissappear, leaving only the fcc diffraction peaks. The fcc peaks are then stable until the arc is extinguished at t=17s, after which the fcc peaks rapidly shift to higher 2θ values as the lattice contracts with cooling. With an additional 1.5 s of cooling, the bcc peaks reappear, and increase in intensity as the weld continues to cool.

The TRXRD results shown in Fig. 9 track the HAZ microstructural evolution in 1045 steel in real time. Using the data presented in this figure, the relative fraction of the bcc and fcc phases present throughout both the heating and cooling cyclse of the weld can be determined. These data, based on measurements of the areas of the x-ray diffraction peaks are plotted in Fig.10.

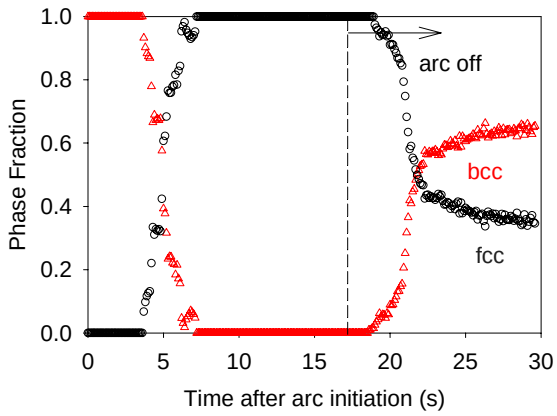

Fig. 10: TRXRD measurements of the relative fraction of the bcc and fcc phases as a function of welding time in 1045 steel.

These results show that the 1045 steel begins to transform to austenite at t=3.6s. The transformation to austenite takes 3.6 seconds to reach completion during the weld heating cycle. The austenite phase is stable until the arc is turned off at t=17.0s, and then continues to be the only phase present for an additional 1.5s while the weld cools. The bcc phase then reappears at t=18.5s, and continues to increase in amount as the fcc→bcc transformation proceeds.

Transformations in 1045 Steel During Rapid Heating. The TRXRD data shown in Fig. 9 were analyzed to determine the relative fractions of the bcc and fcc phases during the welding cycle. The transient weld temperatures for the spot weld were calculated using a procedure described in [11]. The JMA approach was again applied to these data, to determine the kinetic parameters for the $\alpha \rightarrow \gamma$ transformation in the high heating rate spot welds. In these calculations, the JMA equations were discretized and numerically integrated over the calculated heating portion of the weld. The JMA parameters (n, k_0), were then calculated using an activation energy, Q, for the diffusion of carbon in austenite of Q=117.1 kJ/mole [21]. A total of 37 TRXRD data points were used in the calculation, to determine the optimal JMA values of n = 0.82 and ln (k_0) = 12.3 for the 1045 steel.

The results from the 1045 steel study were then compared to those of the 1005 steel study, to determine the differences in transformation kinetics between the two alloys. To do this, the JMA parameters for the 1005 steel were used to predict the fraction austenite for the same time-temperature profile calculated for the 1045 steel weld. The results are superimposed on the 1045 steel results in Fig. 11, where the dashed line represents the predicted transformation for the 1005 steel results, and the solid line represents those for the 1045 steel results.

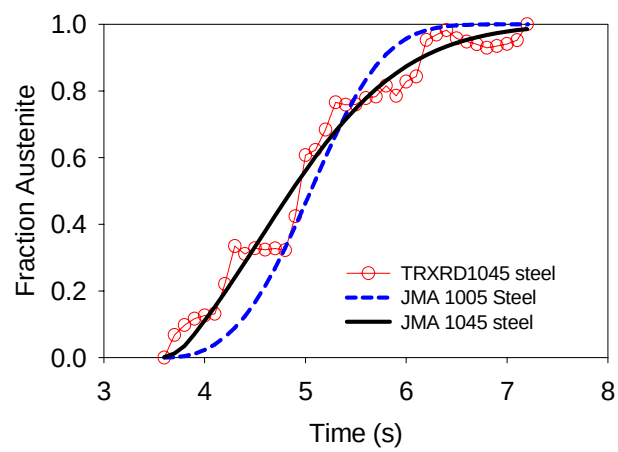

Fig. 11: Kinetics of the ferrite to austenite transformation on weld heating. The TRXRD data for the 1045 steel are given by the circular symbols and solid best-fit line. These results are compared to those of the 1005 steel (dashed line).

Even though the two curves begin at the same time, differences between the two exist. For example, the transformation rate of the 1045 steel is initially somewhat higher than that of the 1005 steel, but slows down to values less than that of the 1005 steel. At approximately 5.5 s after the arc was initiated, the total fraction transformed in each steel is approximately the same (γ=0.75). The higher transformation rate of the 1005 steel at this point allows it to complete the transformation to austenite approximately 1s sooner than that of the 1045 steel.

There are several possible reasons for the differences in the transformation rates for the two steels. First, the different carbon contents of the two steels resulted in different amounts of pearlite in each. In the 1005 steel (Fig. 3) which contained less than 10% pearlite, small pearlite colonies were isolated along the ferrite grain boundaries. In the 1045 steel (Fig. 4) which contained 88% pearlite, the pearlite occupied the majority of the microstructure, leaving a relatively small amount of allotriomorphic ferrite at the prior austenite grain boundaries. The second microstructural difference between the two steels was the starting grain size. Both steels contained equiaxed grains, however, the grain size of the 1045

steel was 92.8 μm, which is more than four times larger than that of the 1005 steel which had a base metal grain size of only 21.5 μm.

The different starting grain sizes and amounts of pearlite in the two steels are responsible for their different transformation rates. Due to the fine dispersion of cementite in the lamellar pearlitic structure, one would expect that the 1045 steel which has the higher fraction of pearlite, to transform more rapidly than the 1005 steel. However, the 1045 steel transforms more rapidly only during the early stages of the transformation, up to γ=0.75. At this point, other factors are coming into play that reduce the overall transformation rate of the 1045 steel relative to that of the 1005 steel.

Another factor which contributes to the different transformation rates is the starting grain size of the two steels. The grain size of the 1045 steel is more than 4 times larger than that of the 1005 steel. It is known that the transformation rate of diffusion controlled reactions will decrease as the grain size gets larger because diffusion is required to take place over larger distances to complete the transformation in the larger grain sized materials [20, 23]. In the 1045 steel, the large amount of pearlite helps to offset the grain size difference by providing numerous nucleation sites within the pearlite. However, the large grain size of the allotriomorphic ferrite regions in the 1045 steel has an indirect effect on the transformation rate. These large ferrite regions should be the last portion of the 1045 steel microstructure to transform, and as such, will control the total amount of time required to completely austenitize the microstructure. Since the allotriomorphic patches in the 1045 steel exceeded 30 μm in places, one might expect that the total time required to transform the 1045 steel would be longer than that of the 1005 steel which had an average grain size of 21.5μm.

Transformations in 1045 Steel During Rapid Cooling The cooling transformations in steel can be more complicated than the heating transformations because of the potential for the formation of non-equilibrium phases at high cooling rates. It is well known that diffusion dependant transformations, such as the formation of pearlite, occur at low cooling rates [24]. As the cooling rate increases, diffusion of carbon may not be rapid enough to allow the lamellar pearlite microstructure to form. Shear-type transformations thus begin to dominate at these higher cooling rates. For example, bainite, which is characterized by a microstructure of mixed ferrite and cementite with non-lameller features, forms through a combination of diffusion and shear at intermediate cooling rates [24]. Martensite, on the other hand, forms entirely by a shear mechanism and only at high cooling rates, producing a microstructure containing lath or plate-like characteristics with the carbon trapped in interstitial sites of the crystal lattice [24]. The formation of bainite and martensite cannot be described by the equilibrium phase diagram, since these transformations occur under non-equilibrium conditions.

Fig. 12 shows the results from one of the 1045 steel TRXRD experiments. This plot shows the 2θ diffraction angle on the x-axis versus time from the beginning of the experiment on the y-axis during cooling of the spot weld. This plot zooms in on the fcc(111) and the bcc(110) diffraction peaks in the HAZ, and shows what happens to the steel after it has been completely transformed to austenite. As soon as the arc is extinguished, the fcc(111) peak rapidly shifts to higher 2θ values as the lattice contracts. At t=22.2s in this plot, the bcc(110) peak first appears during cooling and has a relatively narrow peak width. Both peaks shift to higher 2θ values with continued cooling, and the bcc peak increases in intensity while the fcc peak decreases in intensity. At t=27s in this plot, both the bcc(110) and the fcc(111) peaks show a sudden increase in width. The wider bcc(110) peak exists throughout the remainder of the weld, increasing in intensity as the weld continues to cool, and shifting to slightly higher 2θ values.

The sudden increase in the bcc(110) peak width during cooling was not observed in similar experiments performed on the 1005 steel [3, 8]. The increase in peak width in the 1045 steel can be caused by strain in the lattice, changes in the composition, or changes in the crystal structure. The initial formation of ferrite from austenite, followed by the formation of martensite at lower temperatures would explain the rapid broadening of the bcc diffraction peaks. The martensite would both strain the lattice and create changes in the lattice parameter through the formation of a body centered tetragonal (bct) crystal structure. The strain induced by the martensite would also explain similar changes in the broadening of the austenite peaks that occurred at the same time.

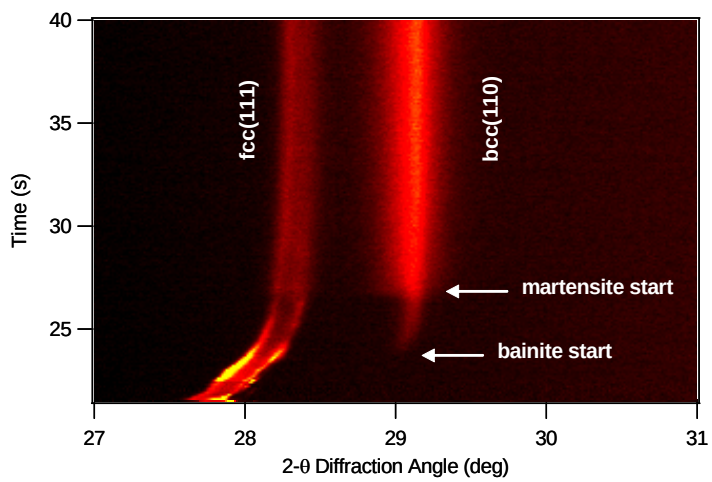

Fig. 12: TRXRD results showing the fcc(111) and bcc(110) diffraction peaks during weld cooling. Martensite formation is accompanied by an increase in peak width.

If martensite is responsible for the peak broadening at low temperatures, there may also be a change in the transformations rates when the martensite begins to form. Additional information is available from the x-ray diffraction peaks that might provide this evidence. Analysis of the

fcc(111) and bcc(110) diffraction peaks was performed to determine the relative fractions of the phases and their lattice parameters as a function of weld cooling time. These results are plotted Fig. 13, where the fraction bcc phase is plotted on the left axis as the black circles, while the bcc lattice parameter is plotted on the right axis as the solid red triangles. Note the difference in the time scales between Fig 12 and Fig 13. Both represent the same data, but Fig. 13 is scaled from the time the arc was extinguished, whereas Fig. 12 was plotted from the beginning of the experiment.

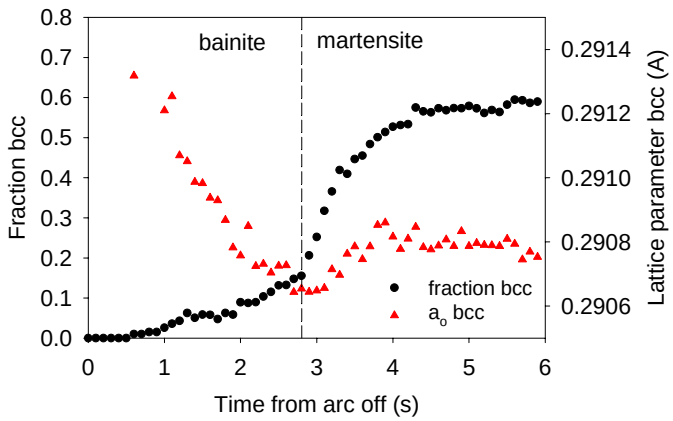

Fig. 13: BCC fraction and lattice parameter as a function of weld cooling time. The transition from bainite to martensite occurs at t=2.8 after the arc was extinguished.

Fig. 13 shows that the first bcc phase appears at t=0.5s after the arc was extinguished. The initial rate of increase in the bcc phase is relatively slow, reaching approximately 15% transformed at t=2.8s. At this time, the bcc peaks rapidly increase in width, leading to a more than 2 times increase in the transformation rate, indicating that there is a change in the transformation mechanism. Such an increase in the transformation rate would not be expected at low temperatures unless a different transformation mechanism occurred. The transformation continues as the temperature decreases, achieving approximately 60% transformed at t=6s after cooling.

Further indications of the martensitic portion of the cooling transformation are provided by changes in the lattice parameters. Fig. 13 also shows how the measured lattice parameters vary with the welding time. A decrease in the bcc lattice parameter is observed during the initial stages of transformation leading up to the change in mechanism at t=2.8s. This behavior would be expected if the initial stage of transformation was occurring by either the formation of bainite since its lattice parameter would decrease as the weld cools. At t=2.8s, when the transformation rate increases, there is an increase in the lattice parameter from 2.906 to 2.908 Å. This increase in lattice parameter is qualitatively consistent with the formation of martensite and provides further evidence that the transformation initiating at t=2.8s is martensitic.

Microstructural observations of the weld HAZ indicate that the final microstructure does indeed contain a mixture of baininte and martensite phases. Fig. 14 shows the microstructure of the HAZ at the location where the TRXRD data were obtained. In this microstructure, the prior austenite grain boundaries in the weld HAZ are much smaller than those in the original base metal as a result of the numerous nucleation sites provided within the original pearlite microstructure. No pearlite is present, and grain boundary ferrite is minimal. The bainitic portions of the microstructure appear as the darker etching patches of localized at the prior austenite grain boundaries. Within the grains, the microstructure is highly refined, and is characteristic of lath martensite that forms during rapid cooling of medium carbon steels [24]. Therefore, the TRXRD results were able to distinguish between martensite and bainite phases based on their transformation rates, lattice parameters and temperatures where they initiated. Additional experiments are planned on higher carbon steels where the effects of carbon on the microstructure will be even more pronounced.

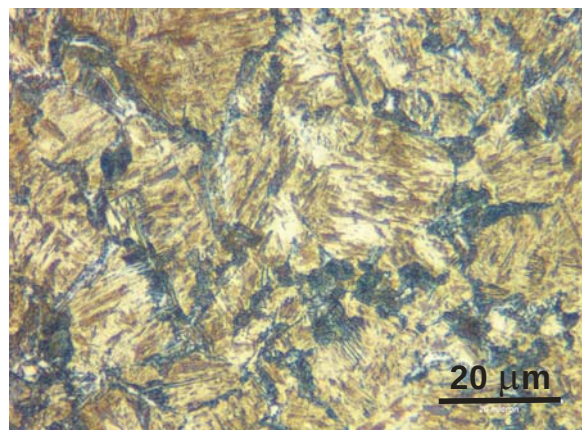

Fig. 14: Photomicrograph of the 1045 steel HAZ, showing a bainitic/martensitic post-weld microstructure.

Conclusions

Synchrotron based x-ray diffraction techniques are providing a new and powerful tool for the study of phase transformations and microstructural evolution during welding. Through several examples of the application of SRXRD and TRXRD methods, it can be seen that these unique experimental tools provide a number of capabilities not previously available to the welding and steel researcher. When combined with additional experiments and modeling, these techniques allow a deeper understanding of the kinetics of phase transformations occurring in the weld metal and HAZ to be gained. As these techniques gain more widespread use, SRXRD and TRXRD will provide the welding research community with the ability to quantitatively describe the kinetics of other prominent phase transformations in many more commercial alloys and improve the knowledge base for the welding of steels and other alloys.

Acknowledgments

This work was performed under the auspices of the U. S. Department of Energy, Lawrence Livermore National Laboratory, under Contract No. W-7405-ENG-48. This work was supported by DOE, Office of Basic Energy Sciences, Division of Materials Science. Portions of this research were carried out at the Stanford Synchrotron Radiation Laboratory, a national user facility operated by Stanford University on behalf of the U.S. Department of Energy, Office of Basic Energy Sciences. The authors would like to express their gratitude to Suresh Babu of the Edison Welding Institute, who provided Igor Pro macros for the analysis of the x-ray data, and Mr. Bob Vallier of LLNL for performing the metallographic characterization of the base metal and welded samples.

References

1. J. W. Elmer, T. A. Palmer and S. S. Babu, "A New Experimental Method for In-Situ Phase Transformation Studies of Steels Using Synchrotron Radiation," *Advanced Materials and Processes*, V160(11), pp. 23-26, 2002.
2. J. W. Elmer, Joe Wong and Thorsten Ressler, "Spatially Resolved X-Ray Diffraction Mapping of Phase Transformations in the HAZ of C-Mn Steel Arc Welds," *Metall. and Mater. Trans. A*, 32A (5), pp. 1175-1187, 2001.
3. Joe Wong, T. Ressler and J. W. Elmer, "Dynamics of Phase Transformations and Microstructure Evolution in C-Mn Steel Arc Welds Using Time Resolved Synchrotron X-Ray Diffraction," *J. Synchrotron Radiation*, 10: pp. 154-167, Part 2, Mar 2003.
4. J. W. Elmer and T. A. Palmer, "In-Situ Monitoring of Phase Transformations During Welding of Steels Using Synchrotron-Based X-Ray Diffraction Techniques," *Proceedings of the 2004 ASME International Mechanical Engineering Congress*, Nov. 13-19, Anaheim, CA, ISBN 0-7918-4180-4, 2004.
5. W. Zhang, J. W. Elmer, and T. Debroy, "An Integrated Modeling Approach toward Understanding of Microstructural Evolution in Arc Welds," in press, *Science and Technology of Welding and Joining*, May, 2005.
6. S. S. Babu, J. W. Elmer, S. A. David and M. Quintana, "In-Situ Observations of Non-equilibrium Austenite Formation During Weld Solidification of a Fe-C-Al-Mn Low Alloy Steel," *Proceedings of the Royal Society: Mathematical, Physical and Engineering Sciences*, 458, pp 811-821, 2002.
7. S. S. Babu, J. W. Elmer, J. M. Vitek, S. A. David, "Time-Resolved X-Ray Diffraction Investigation of Primary Weld Solidification in Fe-C-Al-Mn Steel Welds," *Acta Materialia*, Vol. 50, Iss. 19, pp 4763-4781, 2002.
8. J. W. Elmer, T. A. Palmer, W. Zhang, B. Wood, and T. DebRoy, "Kinetic Modeling of Phase Transformations Occurring in the HAZ of C-Mn Steel Welds Based on Direct Observations," *Acta Materialia*, V51, pp. 3333-3349, 2003.
9. W. Zhang, J. W. Elmer, and T. DebRoy, "Modeling and Real Time Mapping of Phases during GTA Welding of 1005 Steel," *Materials Science and Engineering A*, v 333, issue 1-2, pp 321-335, 2002.
10. W. Zhang, J. W. Elmer, and T. DebRoy, "Kinetics of Ferrite to Austenite Phase Transformation during Welding of 1005 Steel," *Scripta Materialia*, 46, pp753-757, 2002.
11. W. Zhang, G. G. Roy, J. W. Elmer, and T. DebRoy, "Modeling of Heat Transfer and Fluid Flow during GTA Spot Welding of 1005 Steel," *Journal of Applied Physics*, V93(5), pp. 3022-3033, 1 Mar., 2003.
12. Thorsten Ressler, Joe Wong and J. W. Elmer, "Investigation of Real-Time Microstructure Evolution in Steep Thermal Gradients using Spatially Resolved X-ray Diffraction: A Case Study for Ti Fusion Welds," *J. Phys. Chem. B*, 102(52), p. 10724, 1998.
13. T. A. Palmer, J. W. Elmer, and Joe Wong, "In-Situ Observations of Ferrite/Austenite Transformations in Duplex Stainless Steel Weldments Using Synchrotron Radiation," *Science and Technology of Welding and Joining*, 7(3), pp 159-171, 2002.
14. S. Babu, Private communications, Oak Ridge National Laboratory, 2002.
15. K. Mundra, T. DebRoy, and K. Kelkar, *Numerical Heat Transfer*, (29), pp. 115-129, 1996.
16. K. Mundra, J.M. Blackburn, and T. DebRoy, *Sci. Technol. Welding Joining*, 2(4), pp. 174-184, 1997.
17. S. V. Patankar, *Numerical Heat Transfer and Fluid Flow*, Hemisphere Pub. Corp., 1980.
18. J. W. Elmer, T. A. Palmer, S. S. Babu, W. Zhang and T. Debroy, "Direct Observations of Austenite, Bainite, and Martensite Formation During Arc Welding of 1045 Steel using Time Resolved X-ray Diffraction," *Welding Journal*, V83(9), pp 244-s to 253-s, 2004.
19. B. Sundman, B. Jansson and J. Andersson, *Calphad-Computer Coupling of Phase Diagrams and Thermochemistry*, V 9(2), p.153, 1985.
20. J. W. Christian: The *Theory of Transformations in Metals and Alloys, 2nd Edition, Part I*, 1975, Oxford: Pergamon.
21. S. K. Nath, S. Ray, and Mathur VNS, *ISIJ Inter*,v34, p191, 1994.
22. A. Kumar, S. Mishra, J. W. Elmer and T. DebRoy, "Optimization of Johnson Mehl Avrami Equation Parameters for α-Ferrite to γ-Austenite Transformations in Steel Welds using a Genetic Algorithm," *Metallurgical and Materials Transactions A*, 36A (1), pp. 15-22, January 2005.
23. Ø. Grong: Metallurgical Modelling of Welding, *The Institute of Materials*, London, Chapter 1, 1994.
24. G. Krauss: Steels: Heat Treatment and Processing Principles, *ASM International*, Materials Park, OH, 1990.